




# Using Laser Altimetry to Finely Map the Permanently Shadowed Regions of the Lunar South Pole Using an Iterative Self-Constrained Adjustment Strategy

Huan Xie , Senior Member, IEEE, Xiaoshuai Liu, Yusheng Xu, Zhen Ye, Member, IEEE, Shijie Liu , Member, IEEE, Xin Li, Binbin Li, Qi Xu, Yalei Guo, and Xiaohua Tong , Senior Member, IEEE

**Abstract**—Laser altimeters are capable of achieving fine mapping of the permanently shadowed regions (PSRs) of the Moon, which can provide fundamental topographic data for planetary missions. However, various factors can cause uncertainty in the geolocation of laser spots, which in turn causes terrain artifacts. In this article, we present an iterative self-constrained adjustment method to reduce the uncertainty of laser spot positioning. First, grid search was conducted for each altimetric profile from the lunar orbiter laser altimeter (LOLA), to minimize the weighted root-mean-square error (RMSE), constrained by the other altimetric profiles. Second, the updated profiles were iteratively adjusted until the adjustment value for the plane position converged. In addition, statistics from the standardized de-trended slope and residual were created to eliminate outliers, which were indeed some pseudo-topographic observations. In order to validate the results, the deviation of the elevation by projecting the adjusted laser profiles onto the improved LOLA digital elevation model (DEM) were calculated. The mean absolute error between the two is 0.25 m and the RMSE is 0.46 m. For the local terrain features with large differences, high resolution optical images were used for visual interpretation. The analysis shows that the obtained results appear to be more reasonable. Finally, using the corrected LOLA altimetric data, we made a new DEM of the PSRs within 89°S of the lunar south pole, which can provide a refined and reliable topographic dataset for follow-up research.

**Index Terms**—Laser altimetry, lunar orbiter laser altimeter (LOLA), permanently shadowed regions (PSRs), topographic mapping.

## I. INTRODUCTION

**D**UE to the tiny inclination of the Moon's rotation axis, direct sunlight hardly ever reaches some areas of the Moon's

Manuscript received 29 May 2022; revised 31 July 2022; accepted 1 September 2022. Date of publication 7 September 2022; date of current version 21 November 2022. This work was supported in part by the Natural Science Foundation of China under Grant 41822106, Grant 42171432, and Grant 42101447, in part by the Shuguang Program under Grant 18SG22, in part by the Shanghai Science and Technology Project under Grant 21511103800 and Grant 22511102900, in part by the Laboratory of Science and Technology on Aerospace Flight Dynamics under Grant KGJ6142210110305, in part by the Shanghai Municipal Science and Technology Major Project under Grant 2021SHZDZX0100, and in part by the Fundamental Research Funds for the Central Universities. (Corresponding author: Xiaohua Tong.)

The authors are with the College of Surveying and Geo-Informatics, and the Shanghai Key Laboratory for Planetary Mapping and Remote Sensing for Deep Space Exploration, Tongji University, Shanghai 200092, China (e-mail: huanxie@tongji.edu.cn; 14511861xs@tongji.edu.cn; yusheng\_xu@tongji.edu.cn; 89\_yezhen@tongji.edu.cn; liusjtj@tongji.edu.cn; 1931990@tongji.edu.cn; libinbin@tongji.edu.cn; smxj\_xq@tongji.edu.cn; 1933665@tongji.edu.cn; xh-tong@tongji.edu.cn).

Digital Object Identifier 10.1109/JSTARS.2022.3204765

polar regions, which are called permanently shadowed regions (PSRs). Exploration missions and research in recent decades have indicated the possible existence of ice water and volatile substances in the PSRs of the Moon [1], [2], [3], [4], owing to the extreme illumination conditions and low temperatures. These volatile substances could be valuable resources for future lunar missions. Densely distributed in the PSRs of the Moon, craters are always interesting because they not only act as natural “cold traps” for volatiles but also improve our understanding lunar evolution through the study of their geology and morphology. Scholars have focused on several typical lunar craters, such as the Shackleton crater, where it was found that the floor and rim are older than interior walls [5]. The Shoemaker, Cabeus, and Faustini craters, the rims of the Shackleton crater, and the nearby connecting ridge have all been studied in detail as potential lunar landing sites [6], [7], [8], [9]. Although the specific landing sites of individual exploration missions critically depends on the scientific goals and the engineering conditions, there is no doubt that PSRs are attractive for future lunar missions. Future missions such as the Chang'E missions (CE-6, 7, and 8), NASA's Volatiles Investigating Polar Exploration Rover [10], Luna-25, Luna-27, and the Lunar Prospecting Rover [11], [12], [13] intend to investigate the sources of water and volatile substances in the lunar south pole. Furthermore, the National Aeronautics and Space Administration (NASA) of the U.S., the China Lunar Exploration Program, and several other deep space exploration organizations are planning on building a lunar scientific research station for astronaut access, while also conducting collaborative research [14], [15]. The lunar south pole, and especially the PSRs, with their significant scientific value, has been attracting a lot of research interest.

Topography is fundamental and crucial information for in-situ exploration since it provides a reference for exploration mission planning and decision-making [16], [18], [19]. Instead of passive imaging using the Sun as the light source, laser imaging allows the mapping of the PSRs without being dependent on a light source. Consequently, lunar orbiters have almost always been equipped with laser altimeters for topographic mapping and ground control [20], [21], [22], [23]. In the 1970s, the Apollo 11 lunar exploration project of the U.S. took the lead in using an altimeter to carry out lunar ranging [24]. Since then, the use of laser altimeters in the lunar missions of various countries has allowed significant measurements of the lunar surface to be

made and different data products have been derived. In 1994, the Clementine Laser Altimeter was used to map the height of mountains, impact craters, and other terrain on the Moon [20]. In 2007, the CE-1 laser altimeter (LAM) of China collected lunar surface measurements and used them as elevation control points to generate a lunar digital elevation model (DEM) with the image data [25]. In the same year, the Japan Aerospace Exploration Agency launched the SELENE orbiting mission with the Laser Altimeter instrument on board and derived a topographic map of the whole of the Moon [21]. In 2008, India launched the Chandrayaan-1 lunar probe, which was equipped with the Lunar Laser Ranging Instrument, with the aim of measuring the topography and improving the lunar gravity field model [26], [27]. In 2009, the Lunar Orbiter Laser Altimeter (LOLA) on the Lunar Reconnaissance Orbiter (LRO) began operating with a ranging accuracy of 1 m and a precision of 10 cm, and derived a topographic dataset with the highest resolution and accuracy to date [23], [28]. Although laser ranging has the advantage of high precision, the geolocation calibration is particularly important for altimeters because of the uncertainty arising from the quality of the orbital reconstruction and the pointing accuracy, as well as other unexpected factors such as the thermal distortions of LOLA and largely suspending tracking of Kaguya [29], [30], [31], [32]. These uncertainties and errors can also be mapped directly into the high-resolution topographic products as artifacts distributed consistently within the ground tracks.

To reduce the impact of the above factors and improve the quality of topographic data, crossover analysis is one of the most effective approaches. The difference in the crossovers intersected by the ascending and descending altimetric profiles is generally caused by geolocation error, regardless of physical deformation. Constraint equations have been used to minimize the differences of the intersections, to improve the pointing bias of the Mars Orbiter Laser Altimeter [33]. This method has been subsequently applied to lunar altimetric data such as LOLA and CE-1 LAM data [31], [34], [35]. With high-quality topographic data now being available, adjusting the profiles to best fit the reference terrain data is more applicable and is a stronger geometric constraint to correct the bias and improve the quality of the original data [36], [37], [38]. However, most planets have few topographic datasets as prior base maps in deep space exploration missions. Barker et al. [38] improved the LOLA DEM (LDEM) in an innovative self-constrained method using a reduced LDEM as the base map, greatly improving the quality of LOLA altimetry data without auxiliary data. However, when adjusting the altimetric profiles of each batch, the reduced LDEM was generated with all the remaining points, which is redundant to some extent for areas far away from the profiles, as only reference terrain data nearby the target profiles were informative. Furthermore, although Barker divided the laser profiles into batches by randomly selecting, to some extent, it avoided the aggregated distribution of target profiles, however, it hardly ensured that some cases occurred in which the altimeter profiles in some batches are closely distributed, resulting in the inaccuracy of the reduced LDEM as reference terrain because of remaining extremely sparse points.

Therefore, in this article, we propose an improved iterative self-constrained adjustment method. This method no longer requires a prior topographic dataset, but uses the densely distributed points themselves as constraints to eliminate the geolocation errors, as well as minimize the redundancy in the calculation process. Using the proposed method, all the LOLA profiles within  $89^\circ$  of the lunar south pole were adjusted, and the inconsistency of the adjustment values of the profiles at the boundaries was analyzed in the block processing.

## II. DESCRIPTION OF THE STUDY AREA AND EXPERIMENTAL DATA

The study area covers the region  $89^\circ$ – $90^\circ$ S of the lunar south pole. In this area, the terrain undulates greatly, with the elevation span ranging from approximately  $-2.9$  to  $2$  km, and the average slope about  $12.69^\circ$  (with the standard deviation of  $8.79^\circ$ ). There are many impact craters in this area, one of the most well-recognized is the Shackleton crater, with a diameter of approximate 20 km and a depth of more than 4 km. In addition, the de Gerlache and Shoemaker craters with a larger diameter are distributed close to the  $89^\circ$ S latitude. Meanwhile, the PSRs are mostly distributed inside the craters, 15 of which have an area of more than  $1 \text{ km}^2$  [39]. Although the light conditions inside the craters are extremely poor, studies have shown that there can be almost continuous light at the rims of the craters and the connecting ridges, so that these areas may become potential landing sites for future lunar missions.

The LOLA instrument provides the highest-precision lunar altimeter data so far, and it still works in orbit collecting a large number of lunar surface signal points, providing fundamental datasets for current research. The orbital characteristics of the LRO make the ground tracks in the polar regions much denser than those in the low–middle latitudes [40], [41]. The laser pulse repetition frequency of the LOLA instrument is 28 Hz, and each pulse is divided into five beams through a diffractive optic element [28]. Theoretically, 140 spots can be generated on the surface of the Moon per second, ensuring high-density measurement in the polar regions. To date, the LOLA instrument has collected more than 6.9 billion lunar surface observations, of which more than 11 million are distributed within  $89^\circ$ – $90^\circ$ S of the lunar south pole. The measurements are dense enough in the polar regions to allow the proposed self-constrained adjustment process to work.

This study was aimed at generating more refined DEMs and correcting the geolocation error of the raw measurements in the LOLA Reduced Data Record (RDR) products, which result in the topographic artifacts of the OLDEM in the Gridded Data Record products. The OLDEM data product is shown in Fig. 1, where it can be seen that numerous topographic artifacts exist, due to the geolocation errors of the laser spot positioning.

## III. METHOD

Due to the lack of external high-precision auxiliary data, a self-constrained adjustment based on laser spots method is proposed in this article, which makes full use of the dense

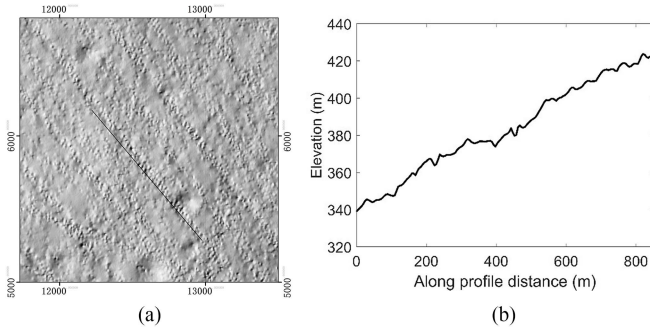


Fig. 1. (a) Close-up shaded relief image of the old LDEM (OLDEM, made from the raw LOLA profiles) in south pole stereographic projection. It can be seen that artifacts are distributed consistently within the ground tracks. (b) Topographic profile along the artifact line [black line in (a)]. The profile is extremely rugged and rough, and is not a portrayal of the real terrain.

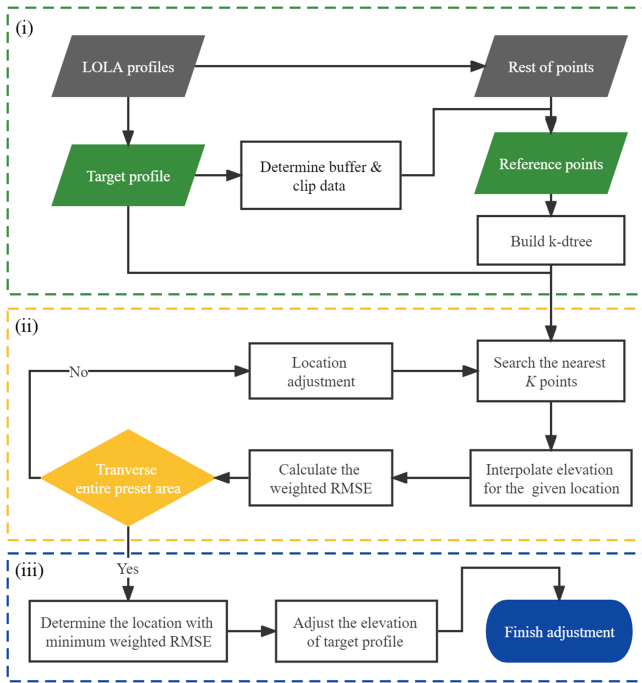


Fig. 2. Flowchart of self-constrained adjustment.

laser spots and treats the closest spots around each profile as the “reference topography”. The individual profiles are then adjusted uniformly within the range of the preset area to make the profiles best fit the reference topography. This process of specific implementation is illustrated in Fig. 2. The adjustment process for the individual LOLA profiles includes three main parts:

- 1) generating the reference terrain dataset;
- 2) adjusting the plane position of the target profile to achieve the best fit with the reference terrain; and
- 3) determining the best fit position and adjusting the elevation values of the target profile.

#### A. Generating Reference Terrain Dataset

Before performing an adjustment of each individual altimetry profile, a dataset of laser spots to use as a reference terrain

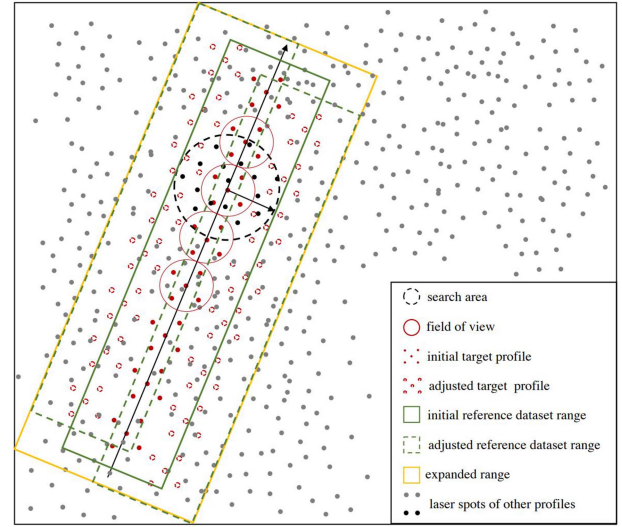


Fig. 3. Range of the reference terrain dataset.

needs to be determined. In fact, since each profile is distributed within a certain range, it is not necessary to use all the remaining laser data as the reference terrain data. Instead, the range of the reference terrain data is determined according to the distribution range of the target profile.

Firstly, the range depends on the size of the search neighborhood used to interpolate the elevation values at the target profile. As depicted in Fig. 3, for each laser spot on the target profile, we need search all nearby laser spots within a radius of 100 m, so the reference data set of the entire target profile must include such a range (green box). In addition, considering that the plane position of each profile will change in the process of adjustment, the range of reference data need to be expanded again to ensure that all spots can be searched within the set area after profile adjustment (yellow box). The laser spots segmented by the above range are used as the reference terrain dataset for the target profile.

Instead of using the laser spots within the searchable range of the current position of the profile (green box), the entire dataset is used to build the  $k$ -d tree (yellow box). The purpose of this is that wherever the position of the target profile is adjusted, the constructed  $k$ -d tree which covers the points in the entire area can directly help to conduct the nearest neighbor search, rather than using the nearby points to reconstruct a  $k$ -d tree when the position changes, which greatly improve computational efficiency.

Local reference datasets are adaptively generated as each altimetry profile is adjusted, which reduces data redundancy compared to generating a global reduced LDEM. Moreover, when using the reduced LDEM as the reference terrain data, it is necessary to first interpolate to achieve rasterization, and then resample the elevation values at the position of the target profile, which introduces a two-step error. However, using the laser spots as the reference terrain data, the elevation values at the target profile can be directly interpolated.

### B. Iterative Adjustment

In this process, considering the footprint size and the range of the field of view of the LOLA instrument, the maximum range of plane location adjustment in the cross- and along-profile directions is set to 50 m. The target profile is adjusted by a step of 2.5 m in both directions, and then a set of elevations is calculated by inverse distance weighted interpolation according to the  $k$  nearest points at each plane location ( $k = 10$  in this study). Note that the step length of the adjustment in the cross- and along-profile directions needs to be transformed into increments in the  $x$ - $y$  directions in the south pole stereographic projection system. The weighted root-mean-square error (RMSE) is used as a metric to evaluate the fit with the reference topography. We adopt the Huber function [41] as the weight function, which determines the weight by calculating the distribution of the elevation residuals. When the residual of an individual spot is within the set threshold, its weight is set to 1, and when it exceeds the set threshold, the weight is set to the reciprocal of the residual. The threshold commonly is set twice the standard deviations of the residuals. In this way, the impact of outliers on the terrain fitting criterion can be effectively reduced. Therefore, each time the laser profile is adjusted, a weighted RMSE value can be calculated. Until the entire preset area is searched, we select the plane position corresponding to the minimum weighted RMSE as the final position.

Fig. 4 depicts how self-constrained adjustment is applied to an individual profile. The colored profiles are the states of the target profile when adjusted to three different plane positions. In Fig. 4(b), A, B, and C correspond to the elevation residual distributions of the laser spots of the adjusted laser profile at three different positions in (a), respectively. It is apparent that the target profile is most consistent with the reference topography when adjusted to the position of the red profile (B).

As the reference topography used in this study was a part of the points to be adjusted, which means that it had errors, the best fitting  $x$ - $y$  position after the process of adjustment was unlikely to be exactly found, but instead approached. Therefore, after adjusting and updating all the profiles, multiple iterations were conducted until the adjustment value of the  $x$ - $y$  position of each profile converged. In general, after four to six rounds of iterations, the plane position adjustment values of the profiles tended to 0. After finishing the iterations, each profile was adjusted to the position that best fitted the topography, which meant that the geolocation bias of the laser profiles was reduced to the greatest extent.

In order to amplify the abrupt features, a detrended slope map was computed as the difference between the actual slope of each pixel and median slope of all the pixels within a certain width window, because the detailed information in the terrain can be highlighted by the detrended topography [43]. The detrended slope map was standardized by the local roughness, aiming to make sure that the large pixel values are due to outliers rather than natural terrain changes [38]. The local roughness was calculated as the median slope at the window size scale [44]. Finally, two statistics for the standardized detrended slope corresponding to each point and for the residuals after the last

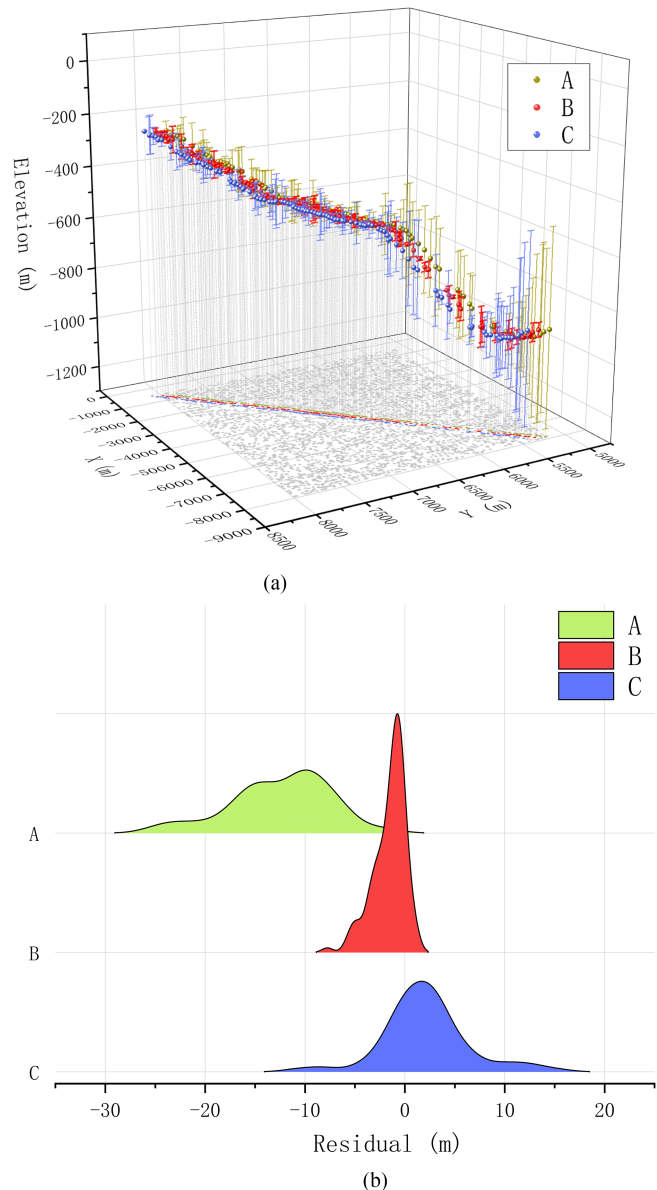


Fig. 4. Topographic residual distribution of an individual profile adjusted to a certain position. (a) Gray points are reference points adjacent to the profile projected on the  $x$ - $y$  plane. The colored points are the spatial distribution corresponding to the three geographic locations (distinguished by color) to which the profile is adjusted. Each point on the profile has an error bar representing the 10 times residuals from the reference topography. (b) Residual distribution plot corresponding to (a).

iteration were constructed to detect and remove the outliers by quantiles.

## IV. RESULTS AND DISCUSSION

### A. Results After Iterative Adjustment and Outlier Removal

To depict the experimental results in detail, we take the area within the yellow box in Fig. 5 as an example. In this area, the elevation span is from  $-2870$  to  $1350$  m. It covers about a quarter of the Shackleton crater, whose dataset consists of 2140 LOLA profiles. These profiles were adjusted by the above method one

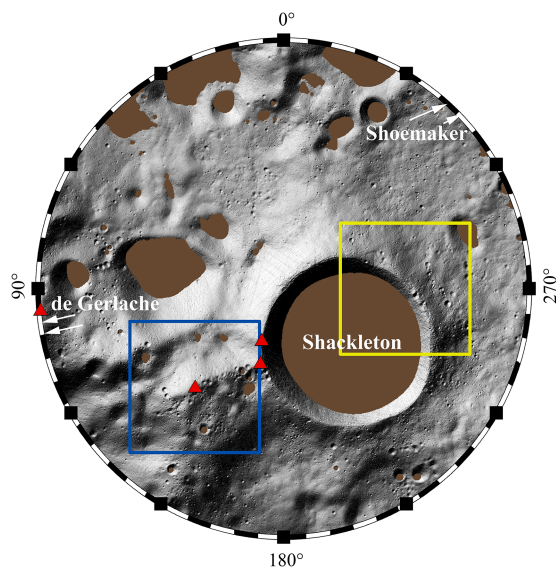


Fig. 5. Relief image of the study area. The base map is the LDEM, and the brown area depicts the extent of the PSRs. The red triangles represent potential landing sites proposed in previous studies [7], [8], [9].

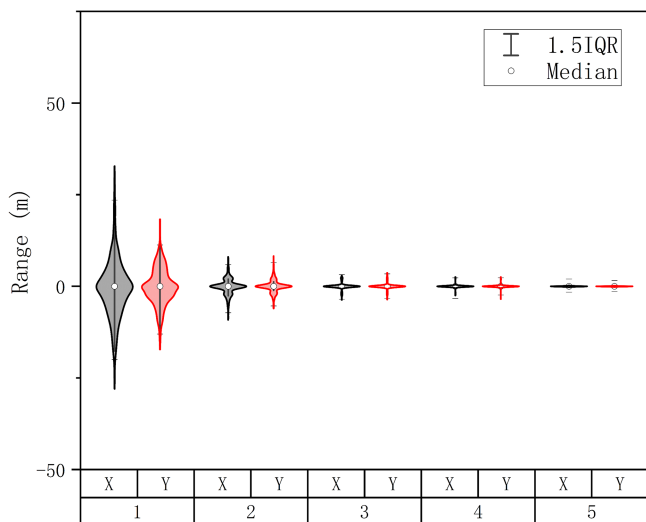


Fig. 6. Results of each round of iterative adjustment. The number in the abscissa represents the iteration times, and the ordinate represents the adjusted value. This value was recorded in the  $x$ - $y$  directions in south polar stereographic projection.

by one, and after five iterations, the planar position of almost every profile converged, as shown in Fig. 6.

After this, the standardized detrended slope and the residuals of the last iteration were used to construct the two statistics  $s_1$  and  $s_2$ . For  $s_1$ , the points outside two sides with the quantiles of 0.1% and 99.9% were removed; for  $s_2$ , we first computed the three times median absolute deviation as a criterion to pick the points with large residuals, and then removed the points outside the two sides with the quantiles of 0.1% and 99.9%. In total, the process yielded about 3700 outliers out of over 1.01 million points in this tile.

The DEM in this study is created using the tool “Generic Mapping Tools” as same as OLDEM. Fig. 7 shows the close-up

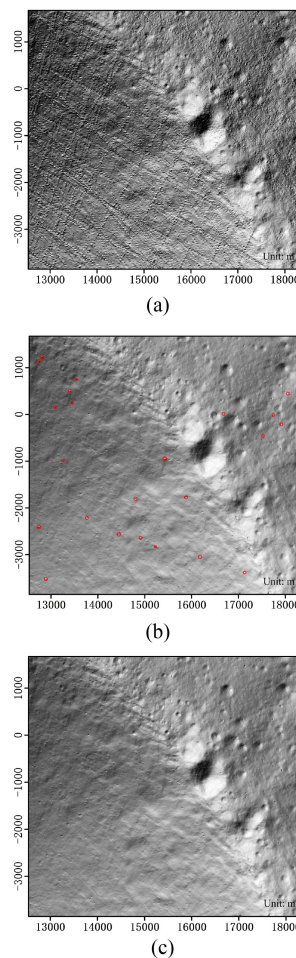


Fig. 7. Close-up shaded relief image of part of the Shackleton crater. (a) OLDEM. (b) and (c) PLDEM derived from the processed LOLA spots before and after outlier removal, respectively. The red circles in (b) represent several pseudo-features caused by outliers.

shaded relief image of part of the Shackleton crater. Before the processing, there were many artifacts in the OLDEM, which can obscure the real terrain details. After applying the proposed algorithm to the raw LOLA profiles, the geolocation error of the laser spots was reduced so that the many artifacts in the processed DEM (PLDEM, made from the processed LOLA profiles) were removed.

The removal of artifacts is not only an optimization of the visual effect but, more importantly, is a correction of the terrain data, which is confirmed in Figs. 8 and 9. In Fig. 8, we resampled the topographic profiles from the OLDEM and the PLDEM derived from the processed profiles along random artifacts, respectively. By comparison, it is found that the difference in elevation reaches several tens of meters in the steep areas, such as the pit wall. Likewise, differences in the elevation affect differences in the slope. As shown in Fig. 9, the slope map obtained from the OLDEM has obvious linear distribution artifacts, and the slope changes of the adjacent artifacts are very abnormal. In contrast, these phenomena do not exist in the new slope map.

Finally, the proposed method was used to process the altimetric profiles in this area and a topographic map was derived, as

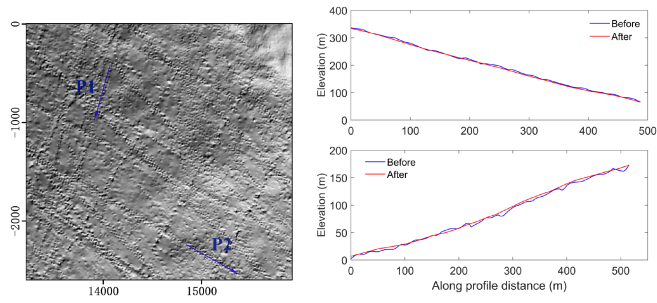


Fig. 8. Profiles resampled from the OLDEM and PLDEM.

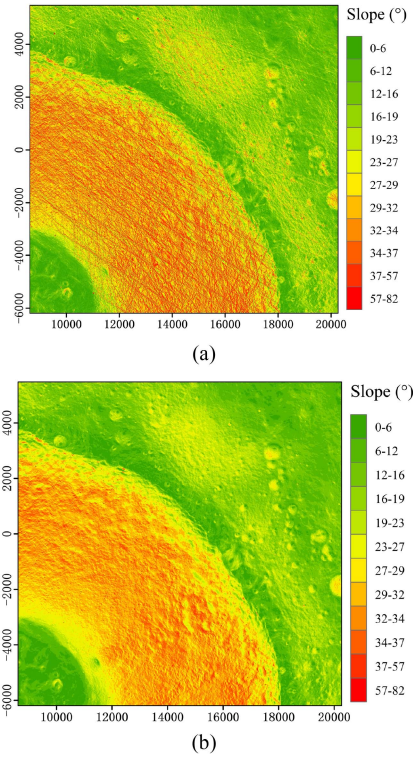


Fig. 9. Terrain slope maps (a) before and (b) after processing.

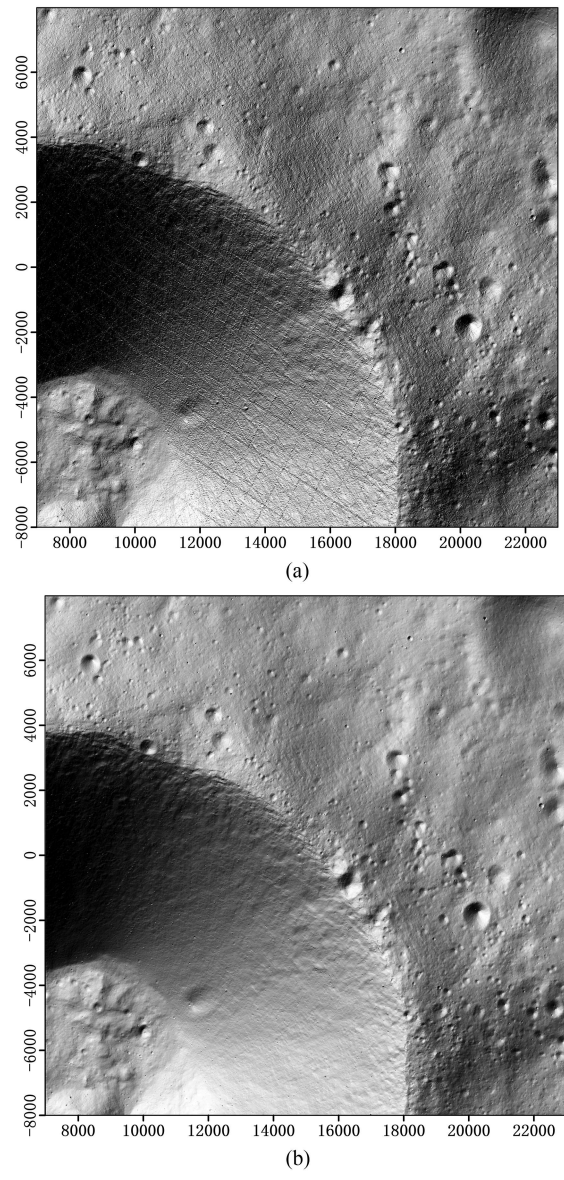


Fig. 10. Topographic maps from (a) the OLDEM and (b) the PLDEM.

shown in Fig. 10. Clearly, the many terrain artifacts have been successfully removed.

**B. Verification of the Results**

The correctness of the results was verified through comparing the results obtained in this study with the new LDEM (NLDEM) of site 01 (the area within the blue box in fig. 5) released by Barker et al. [38] (available at <https://pgda.gsfc.nasa.gov/products/78>), for which the vast majority of the streaky artifacts have been removed. First, the mean absolute error (MAE) and RMSE were calculated by comparing the corrected LOLA points with the NLDEM. Second, the topographic profiles were resampled from the OLDEM, NLDEM, and PLDEM obtained in this study to compare the differences. The results are shown in Figs. 11 and 12.

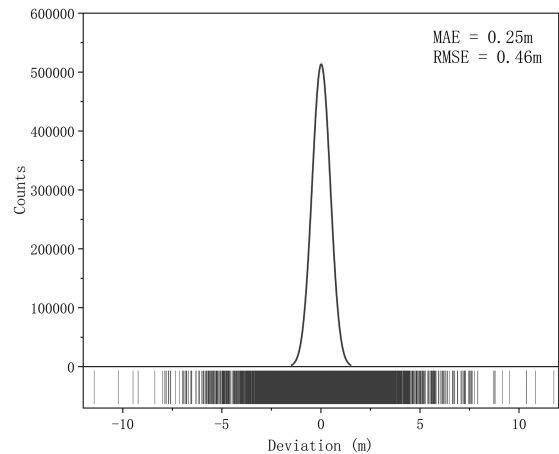


Fig. 11. Deviation of the adjusted LOLA points and the NLDEM.

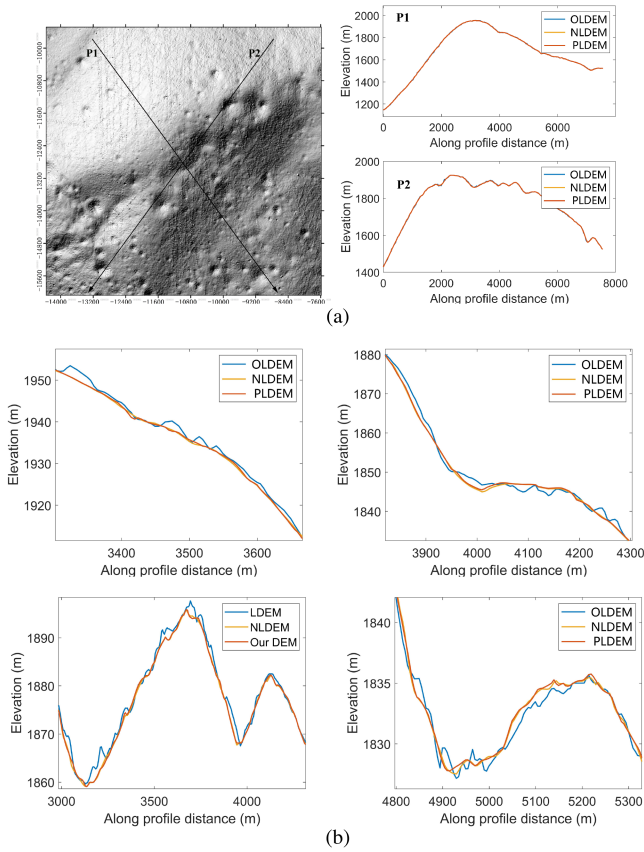


Fig. 12. Topographic profiles illustrating the consistency of the three DEMs. (a) Two topographical profiles P1 and P2 and their positions on the OLDEM. (b) Top two are the partial enlarged views of P1 and the bottom two are the partial enlarged views of P2.

After iterative adjustment, the LOLA points of the results obtained in this study were projected to the NLDEM. We sampled the elevation values at the location of each point from the NLDEM and computed the deviation of the elevation between the adjusted points and the sample dataset. The MAE is 0.25 m and the RMSE is 0.46 m. It can therefore be concluded that the adjusted points of the results obtained in this study are in good agreement with the NLDEM.

The topographic profiles which cross the ridge near to the Shackleton crater were resampled from the three DEMs, as shown in Fig. 11. The topographic profiles from PLDEM differ significantly from the OLDEM; however, this difference is reasonable because they maintain a close fit with the topographic profiles of the NLDEM.

### C. Detailed Analysis of Different Terrain Features

As the deviation of a minority of the adjusted points and the NLDEM reaches up to several meters, as shown in Fig. 11, several distinct features from the NLDEM and the PLDEM were analyzed in detail.

The LROC NAC images and the LROC NAC DEM (NACDEM) generation from stereo pairs over the lunar south pole (available on [https://astropedia.astrogeology.usgs.gov/download/Moon/LRO/MOON\\_LRO\\_NAC\\_DEM\\_89S210E\\_](https://astropedia.astrogeology.usgs.gov/download/Moon/LRO/MOON_LRO_NAC_DEM_89S210E_)

4mp.tif) were used as the auxiliary data because they have a higher resolution of 0.5–2.0 m and 4.0 m, which can effectively help us to visually distinguish the authenticity of some of the features. Fig. 13 shows that three sites (A, B, and C) show different characteristics in (a) the NLDEM and (b) the PLDEM. By projecting the points removed by the proposed algorithm (represented by the red circles) in the NLDEM and the geo-registered LROC NAC image shown in Fig. 13(e), it can be seen that the main reason for the difference can be attributed to the fact that some points in these areas are regarded as outliers during the processing of the proposed algorithm, so that some actual holes and protrusions do not exist in the PLDEM. By a visual comparison with (c) the NACDEM and (d) LROC NAC images, we did not find such features corresponding to the positions of these laser spots. Meanwhile, the topographic profiles across these features were generated to illustrate the differences, as shown in Fig. 13(f). While the topographic profiles sampled from the PLDEM are in close agreement with the topographic profiles sampled from the OLDEM and the NACDEM, it is obvious that the PLDEM trends are more consistent with the OLDEM and the NACDEM topographic where there are significant differences. As for site C, the protrusion appears to be more of a pseudo-feature, as it is distributed on the relatively smooth inner wall of the crater and does not match the general trend of the terrain, which can be proved by the topographic profile of the NACDEM. Furtherly, we simulated the lighting conditions at this moment of the observation time of the LROC NAC image, and rendered NLDEM and PLDEM for a clearer visual inspection of the three sites shown in Fig. 13(g). The results are consistent with the above analysis.

### D. Block Processing

We divided all the RDR data in the study area into 18 blocks. As individual profiles could be truncated into different blocks, this would mean that the adjustment results among the different blocks for one profile may be different. In order to reduce the inconsistency as much as possible, we considered the division of the regions in detail. Specifically, the small topographic features with large fluctuations were divided into the same block as much as possible. As for features with a large spatial size, partial integrity within separate blocks was required. The implementation result of the specific block scheme is shown in Fig. 14. The purpose was to avoid misjudging the real features with large fluctuations as outliers during the adjustment process.

In the process of iterative adjustment, an entire altimetric profile could be divided into different blocks and adjusted with reference to different terrain. In theory, the adjustment values should be very close. However, due to the uncertainty of other factors and the difference in the reference terrain, the adjustment of different parts of the same laser altimetric profile can be different.

A and B in Fig. 15(a) are the PLDEMs generated from the laser data processed with the proposed method. The size of the overlapping area between A and B is 1 km × 12 km, and a total of 1036 profiles are found within the overlapping area. Since the

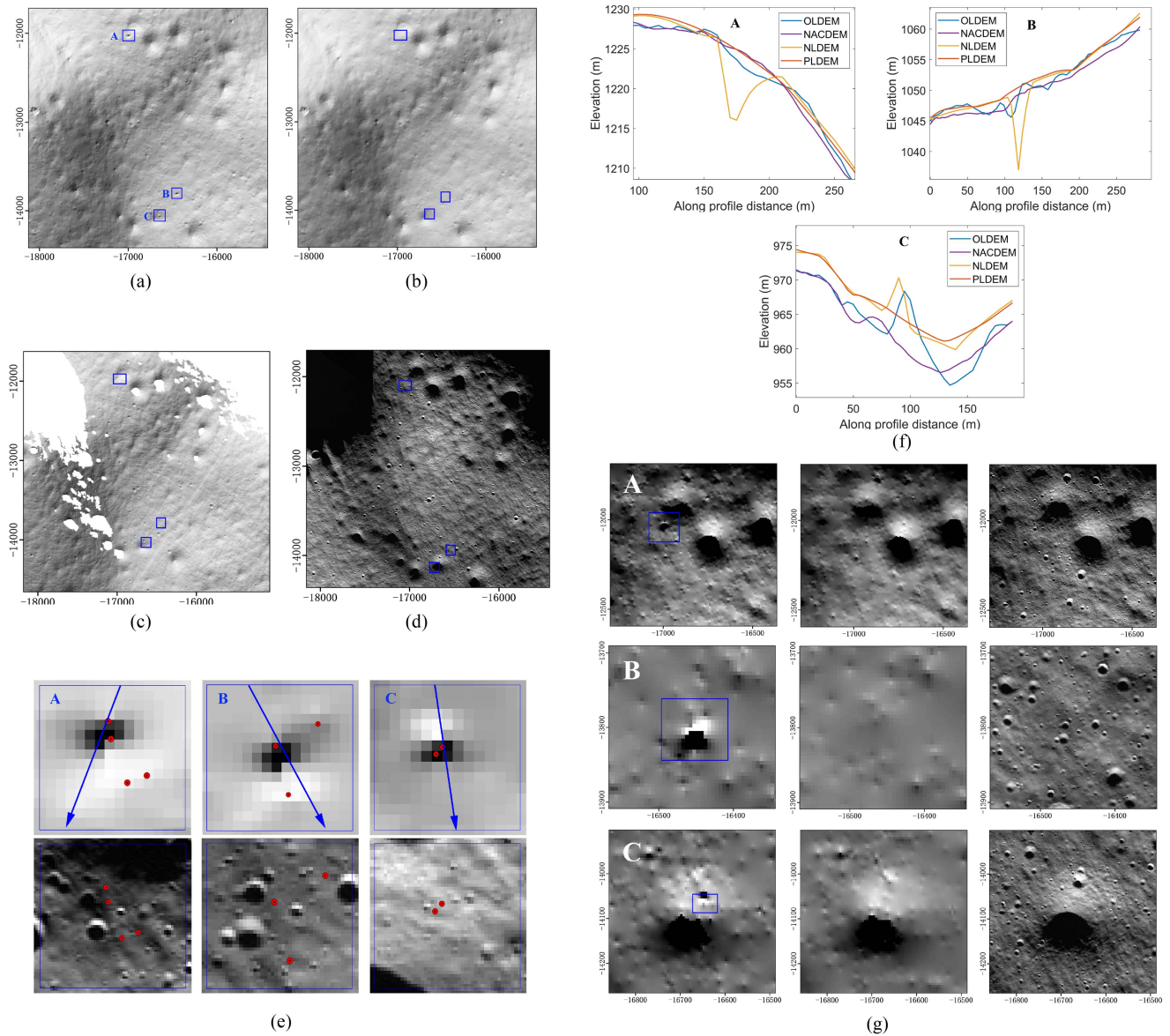


Fig. 13. Illustration of the different ground features in (a) the NLDEM and (b) the PLDEM obtained in this study, where the elevation deviation reaches approximately 10 m. There are two obvious holes for sites A and B and a protrusion for site C in the NLDEM, which are not seen in the PLDEM. (c) Geo-registered pair of LROC NAC images tm146155065re\_cal and tm146155065le\_cal. (d) NACDEM generation from LROC stereo pairs with the resolution of 4 m. The points removed by the proposed algorithm (represented by the red circles) were projected to the geo-registered LROC NAC image shown as (e). The topographic profiles across these features were generated to illustrate the differences as shown in (f). (g) Lighting renderings of NLDEM (left) and PLDEM (mid) compared to LROC NAC image (right).

reference topographic data are inconsistent, when the common altimetric profiles are adjusted iteratively with self-constrained adjustment in the different blocks, the final adjustment result will have a slight deviation. In Fig. 15(b), the adjustment values of the common profiles are presented. It can be found that the adjustment values of most of the profiles in the  $x$ - $y$  directions are basically the same, and only a few profiles show differences. The panel in Fig. 15(c) shows the distribution of the laser profile data in the overlapping area, and the color bar represents the deviation of the adjustment values of the profiles in A and B. The laser profiles with a large deviation are distributed at the edge of the overlapping area, which indicates that the difference in the adjustment results is mainly caused by the uneven distribution

of the laser profiles in A and B. In view of this problem, after adjusting all the laser profiles, for the profiles those were divided into different blocks in the overlapping area with large differences in the results in the overlapping area, we chose the result of the area with a larger distribution range for the laser profile of the track as the final adjustment result. This was done because, for the large span of the public laser profile, the number of points involved in the geometric constraint is greater.

Through the above processing strategy, the possible inconsistency in the overlapping area was minimized, ensuring that no seams would appear when the terrain data were spliced, and the terrain features at the splicing would be perfectly matched, to ensure completeness and consistency (Fig. 16).



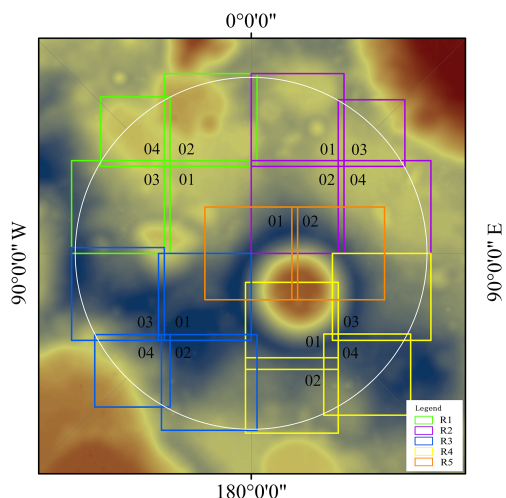


Fig. 14. Data blocks covering 89°–90°S, with the OLDDEM as the base map. The boxes in different colors represent different regions, and each region is divided into several blocks. Pairwise overlaps between blocks are used to verify the consistency of the results.

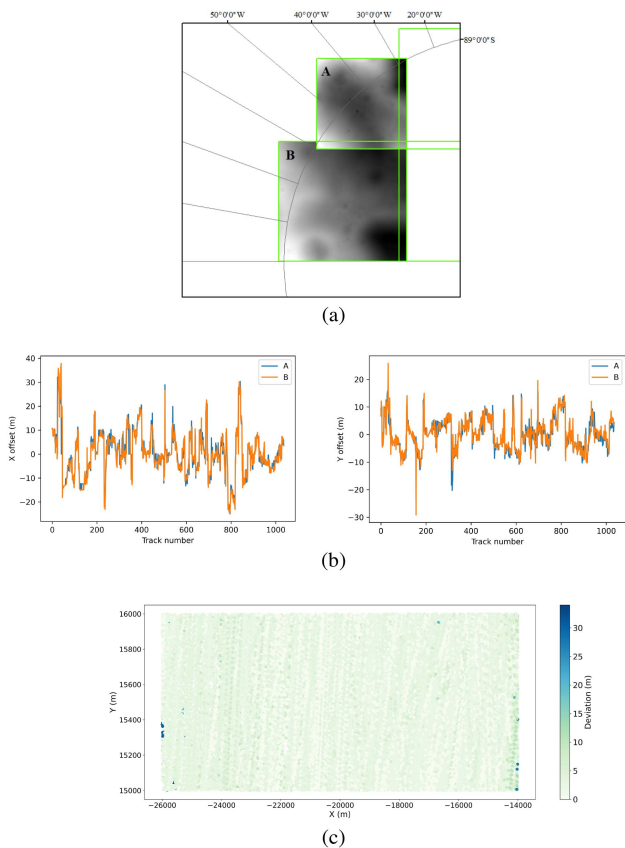


Fig. 15. Statistics for the adjustment values of the public laser profile in the overlapping area.

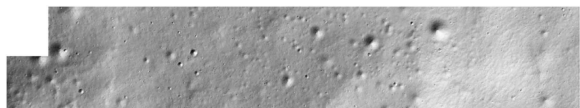


Fig. 16. Shaded relief image of the overlapping region.

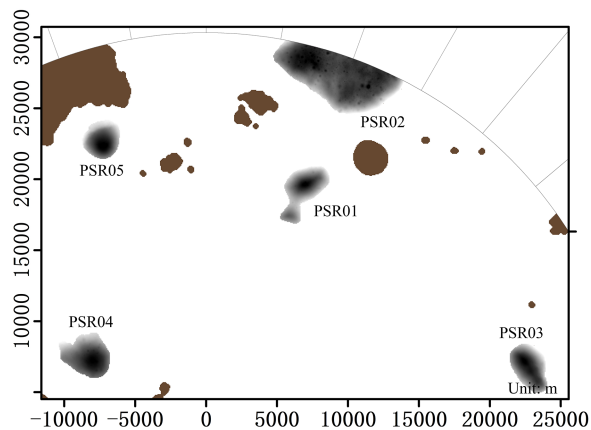


Fig. 17. Distribution map for the five independent PSRs.

TABLE I  
DETAILS OF THE REGIONS AND DATA VOLUMES

Region	Block	Area (km <sup>2</sup> )	Track amount	Spot amount
R1	01	15×16	2536	1077868
	02	16×16	2795	1101596
	03	17×16	2205	1068857
	04	12×12	1908	681382
R2	01	16×16	2754	1094604
	02	16×16	2601	1148595
	03	11.5×11.5	1651	508415
	04	16×16	1859	709306
R3	01	16×15	2294	957048
	02	16.5×15.5	2378	986020
	03	16×16	1774	711434
	04	13×12.5	1380	378244
R4	01	16×15	2407	1004833
	02	16×13	2226	750254
	03	17×15	1874	764380
	04	15×14	2077	794894
R5	01	16×16	2362	920870
	02	16×16	2140	942547

Five independent PSRs, as shown in Fig. 17 and listed in Table I, were selected to compare the PLDEM obtained in this study with the NLDEM, to verify the validity of the results. The DEM of difference (DoD) maps show the deviation of the two (see Fig. 18). In general, the deviation is random, and most of the differences are within 1 m. The deviation of a few pixels reaches several meters, which is mainly due to the different processing strategies for the outliers, as per the previous analysis.

In the PSRs, the overall consistency between the PLDEM and the NLDEM is still high. Through the statistics of the DoD map, it can be seen from the distribution histograms (see Fig. 19) that there are only a few pixels with an elevation difference of more than 2 m, and most of the deviations are at the decimeter level. At the same time, the MAE and RMSE in the five regions were calculated to quantitatively characterize the overall consistency. The specific results are listed in Table II.

It can be seen from Table II that the results for PSR01 and PSR05 are slightly worse than those for the other three regions.

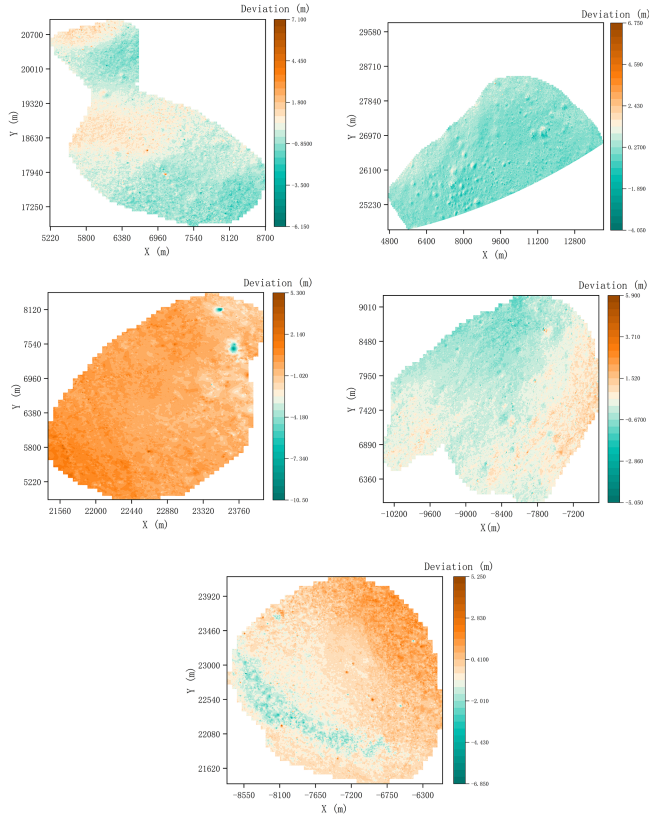


Fig. 18. DoD maps between the PLDEM and the NLDEM.

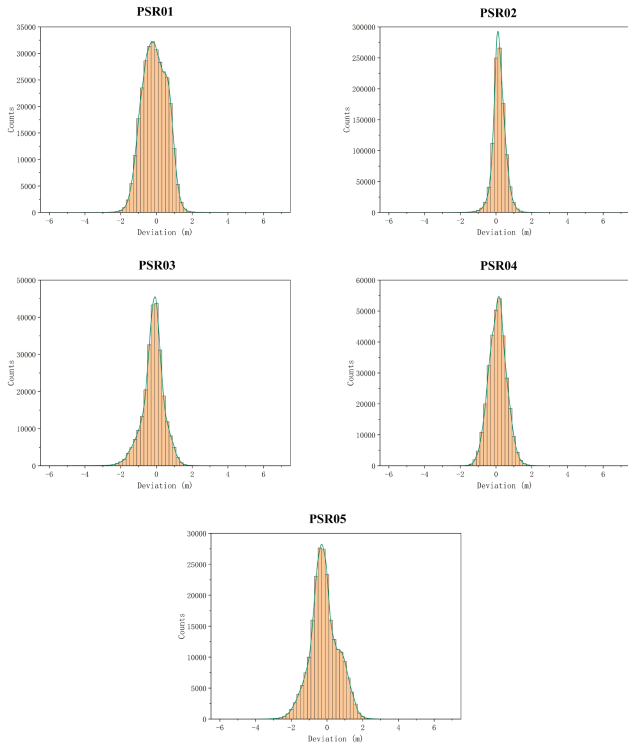
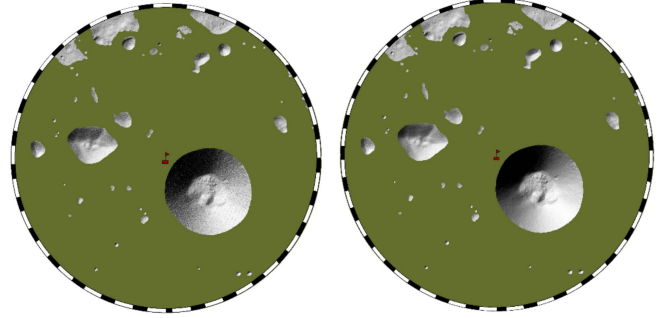


Fig. 19. Histograms of deviation.

TABLE II  
STATISTICS OF THE DEVIATION OF THE NLDEM AND PLDEM

Region	MAE (m)	RMSE (m)
PSR01	0.56	0.69
PSR02	0.30	0.40
PSR03	0.48	0.69
PSR04	0.40	0.51
PSR05	0.63	0.80

Fig. 20. Topographic map of the PSRs within  $89^\circ$  of the lunar south pole. The left is the OLDEM product, and the right is the PLDEM product generated from the LOLA laser profiles processed by the proposed algorithm.

The main reason for this is that there are more different topographic features in these two regions, which has an impact on the quantitative metrics. On the whole, the PLDEM obtained in this study can be considered as reliable, and the existing differences will need further research or quantitative verification and analysis, with the assistance of higher-precision data.

Finally, the LOLA laser data within  $89^\circ$ S of the lunar south pole were all processed to finally regenerate the DEM dataset. According to the distribution range of the PSRs, a topographic map was generated. As shown in Fig. 20, the left image is based on the OLDEM product released by NASA, and the right image is from the PLDEM generated from the LOLA altimetric profiles processed by the algorithm proposed in this article. It can be seen that the quality of the topographic map has been greatly improved.

## V. CONCLUSION

In this article, we have introduced an iterative self-constrained adjustment method to eliminate the geolocation errors of laser spots. Owing to the dense distribution of the LOLA points, strong geometric constraints were constructed between the points themselves, without relying on external high-precision terrain data.

In order to construct the constraints, the elevation at the target point location needed to be calculated from the reference terrain data and then compared with the real measurement value. Compared to using a “reduced LDEM,” the strategy of directly using the adjacent points as the reference terrain data has some advantages. The former strategy requires interpolation to first generate the DEM, and then the elevation values are resampled, while the latter strategy involves direct interpolation of the elevation value of the target position, reducing the additional error introduced

in the calculation process. In addition, the track-by-track adjustment is more reliable than batch adjustment because it ensures that there will always be sufficient real observation data near the target to be adjusted as the reference terrain, avoiding the errors in the reference terrain due to the concentrated distribution of batch data. Finally, for the adjustment of each profile, only adjacent local points need to be used instead of generating global terrain, which reduces the computational redundancy.

The weighted RMSE was used as the objective function, and the Huber function as the weight function was used to reduce the interference of outliers on the results. Iterations were performed until the adjusted value of the position converged toward 0, to ensure that each laser profile was correctly adjusted to the position that best fitted the terrain. After this, the standardized detrended slope and the elevation residuals of the last iteration were used to construct statistics to filter out some of the outliers that would cause abnormal protrusions or holes in the DEM.

Furthermore, we compared the processed points and the PLDEM obtained in this study with the NLDEM released by NASA, and the results showed that the two are in good agreement. Especially in the areas where there is a great difference with the OLDEM, the results obtained in this study are consistent with the NLDEM. However, when compared with LROC NAC images and the NACDEM for some differences between NLDEM and the PLDEM, it seems that the results obtained in this study are more reasonable. Finally, a PLDEM dataset covering the 89°S latitude was produced by block processing. We generated the topography of the PSRs within 89° of the lunar south polar derived by the processed and original laser altimetric profiles of LOLA.

Overall, the iterative self-constrained adjustment proposed in this article can greatly improve the quality of the topography measurements. The improvement was illustrated by processing the altimetric profiles into topographic maps with the many artifacts removed. We analyzed the results by quantitative comparison with NLDEM and visual inspection assisted with LROC images, however, did not estimate the uncertainty as Barker et al. did, which was enlightening for our future work. In addition, we will carry out follow-up studies based on the results of this study, such as an analysis of the lighting conditions in future work. At the same time, we will attempt to apply the proposed method to the processing of laser altimetry data from subsequent planetary exploration missions.

#### ACKNOWLEDGMENT

The authors would like to thank NASA for releasing the LRO science data used in this study, which are available at the Planetary Data System Geosciences Node (<https://pds-geosciences.wustl.edu/missions/lro/lola.htm>).

#### REFERENCES

- [1] E. A. Fisher et al., "Evidence for surface water ice in the lunar polar regions using reflectance measurements from the lunar orbiter laser altimeter and temperature measurements from the diviner lunar radiometer experiment," *Icarus*, vol. 292, pp. 74–85, Apr. 2017, doi: [10.1016/j.icarus.2017.03.023](https://doi.org/10.1016/j.icarus.2017.03.023).
- [2] S. Li et al., "Direct evidence of surface exposed water ice in the lunar polar regions," *Proc. Nat. Acad. Sci.*, vol. 115, no. 36, 2018, Art. no. 8907, doi: [10.1073/pnas.1802345115](https://doi.org/10.1073/pnas.1802345115).
- [3] B. A. Cohen, P. O. Hayne, B. Greenhagen, D. A. Paige, C. Seybold, and J. Baker, "Lunar flashlight: Illuminating the lunar South Pole," *IEEE Aerosp. Electron. Syst. Mag.*, vol. 35, no. 3, pp. 46–52, Mar. 2020, doi: [10.1109/maes.2019.2950746](https://doi.org/10.1109/maes.2019.2950746).
- [4] A. N. Deutsch, J. W. Head, and G. A. Neumann, "Analyzing the ages of south polar craters on the Moon: Implications for the sources and evolution of surface water ice," *Icarus*, vol. 336, 2020, Art. no. 113455, doi: [10.1016/j.icarus.2019.113455](https://doi.org/10.1016/j.icarus.2019.113455).
- [5] M. T. Zuber et al., "Constraints on the volatile distribution within Shackleton crater at the lunar south pole," *Nature*, vol. 486, no. 7403, pp. 378–381, Jun. 2012, doi: [10.1038/nature11216](https://doi.org/10.1038/nature11216).
- [6] M. Lemelin, D. M. Blair, C. E. Roberts, K. D. Runyon, D. Nowka, and D. A. Kring, "High-priority lunar landing sites for in situ and sample return studies of polar volatiles," *Planet. Space Sci.*, vol. 101, pp. 149–161, Oct. 2014, doi: [10.1016/j.pss.2014.07.002](https://doi.org/10.1016/j.pss.2014.07.002).
- [7] J. Flahaut et al., "Regions of interest (ROI) for future exploration missions to the lunar South Pole," *Planet. Space Sci.*, vol. 180, 2020, Art. no. 104750, doi: [10.1016/j.pss.2019.104750](https://doi.org/10.1016/j.pss.2019.104750).
- [8] Z. He et al., "Proposals for lunar south polar region soft landing sites selection," *J. Deep Space Exploration*, vol. 7, no. 3, pp. 232–240, 2020, doi: [10.15982/j.issn.2095-7777.2020.20191003002](https://doi.org/10.15982/j.issn.2095-7777.2020.20191003002).
- [9] D. De Rosa et al., "Characterisation of potential landing sites for the European space agency's lunar lander project," *Planet. Space Sci.*, vol. 74, no. 1, pp. 224–246, Dec. 2012, doi: [10.1016/j.pss.2012.08.002](https://doi.org/10.1016/j.pss.2012.08.002).
- [10] A. Colaprete et al., "An overview of the volatiles investigating polar exploration rover (viper) mission," in *Proc. AGU Fall Meeting Abstr.*, vol. 2019, 2019, pp. P34B–P303.
- [11] I. Mitrofanov, L. Zelenyi, and V. Tret'yakov, "Upgraded program of Russian lunar landers: Studying of lunar poles," in *Proc. Annu. Meeting Lunar Exploration Anal. Group, Lunar Planet. Inst.*, 2015, Paper 3025.
- [12] J. Liu et al., "Landing site selection and overview of China's lunar landing missions," *Space Sci. Rev.*, vol. 217, no. 1, pp. 1–25, 2021, doi: [10.1007/s11214-020-00781-9](https://doi.org/10.1007/s11214-020-00781-9).
- [13] J. Carpenter, R. Fisackerly, S. Aziz, and B. Houdou, "Exploring cold trapped volatiles from stationary landers and mobile rovers: ESA activities for resource prospecting at the Poles," in *Proc. Annu. Meeting Lunar Exploration Anal. Group*, vol. 1863, 2015, Paper 2027.
- [14] C. Li, C. Wang, Y. Wei, and Y. Lin, "China's present and future lunar exploration program," *Science*, vol. 365, no. 6450, pp. 238–239, 2019, doi: [10.1126/science.aax9908](https://doi.org/10.1126/science.aax9908).
- [15] NASA, "NASA seeks US partners to develop reusable systems to land astronauts on Moon," [Online]. Available: <https://www.nasa.gov/feature/nasa-seeks-us-partners-to-develop-reusable-systems-to-land-astronauts-on-moon/> (accessed
- [16] C. I. Fassett et al., "Lunar impact basins: Stratigraphy, sequence and ages from superposed impact crater populations measured from lunar orbiter laser altimeter (LOLA) data," *J. Geophys. Res., Planet.*, vol. 117, no. E12, Dec. 2012, doi: [10.1029/2011JE003951](https://doi.org/10.1029/2011JE003951).
- [17] A. Johnson, J. Hoffman, D. Newman, E. Mazarico, and M. Zuber, "An integrated traverse planner and analysis tool for planetary exploration," in *Proc. AIAA SPACE Conf. & Expo.*, 2010, Art. no. 8829.
- [18] N. J. Potts et al., "Robotic traverse and sample return strategies for a lunar farside mission to the Schrödinger basin," *Adv. Space Res.*, vol. 55, no. 4, pp. 1241–1254, Feb. 2015, doi: [10.1016/j.asr.2014.11.028](https://doi.org/10.1016/j.asr.2014.11.028).
- [19] W. Hao, C. Zhu, F. Li, J. Yan, M. Ye, and J.-P. Barriot, "Illumination and communication conditions at the Mons Rümker region based on the improved lunar orbiter laser altimeter data," *Planet. Space Sci.*, vol. 168, pp. 73–82, Apr. 2019, doi: [10.1016/j.pss.2019.01.010](https://doi.org/10.1016/j.pss.2019.01.010).
- [20] D. E. Smith, M. T. Zuber, G. A. Neumann, and F. G. Lemoine, "Topography of the Moon from the Clementine lidar," *J. Geophys. Res., Planet.*, vol. 102, no. E1, pp. 1591–1611, 1997, doi: [10.1029/96JE02940](https://doi.org/10.1029/96JE02940).
- [21] H. Araki et al., "Lunar global shape and polar topography derived from Kaguya-LALT laser altimetry," *Science*, vol. 323, no. 5916, pp. 897–900, Feb. 2009, doi: [10.1126/science.1164146](https://doi.org/10.1126/science.1164146).
- [22] S. Huixian, D. Shuwu, Y. Jianfeng, W. Ji, and J. Jingshan, "Scientific objectives and payloads of Chang'E-1 lunar satellite," *J. Earth Syst. Sci.*, vol. 114, no. 6, pp. 789–794, Dec. 2005, doi: [10.1007/BF02715964](https://doi.org/10.1007/BF02715964).
- [23] D. E. Smith et al., "The lunar orbiter laser altimeter investigation on the lunar reconnaissance orbiter mission," *Space Sci. Rev.*, vol. 150, no. 1–4, pp. 209–241, 2009, doi: [10.1007/s11214-009-9512-y](https://doi.org/10.1007/s11214-009-9512-y).

- [24] J. O. Dickey et al., "Lunar laser ranging - A continuing legacy of the Apollo program," *Science*, vol. 265, no. 5171, pp. 482–490, Jul. 1994, doi: [10.1126/science.265.5171.482](https://doi.org/10.1126/science.265.5171.482).
- [25] C. Li, X. Ren, J. Liu, and X. Zou, "Laser altimetry data of Chang'E-1 and the global lunar DEM model," *Sci. China Earth Sci.*, vol. 40, no. 3, pp. 281–293, 2010, doi: [10.1007/s11430-010-0054-7](https://doi.org/10.1007/s11430-010-0054-7).
- [26] J. N. Goswami and M. Annadurai, "Chandrayaan-1: India's first planetary science mission to the moon," *Curr. Sci.*, vol. 96, no. 4, pp. 486–491, Feb. 2009.
- [27] J. A. Kamalakar et al., "Lunar laser ranging instrument (LLRI): A tool for the study of topography and gravitational field of the Moon," *Curr. Sci.*, vol. 96, no. 4, pp. 512–516, Feb. 2009.
- [28] D. E. Smith et al., "Initial observations from the lunar orbiter laser altimeter (LOLA)," *Geophys. Res. Lett.*, vol. 37, no. 18, 2010, doi: [10.1029/2010gl043751](https://doi.org/10.1029/2010gl043751).
- [29] D. E. Smith et al., "Summary of the results from the lunar orbiter laser altimeter after seven years in lunar orbit," *Icarus*, vol. 283, pp. 70–91, 2017, doi: [10.1016/j.icarus.2016.06.006](https://doi.org/10.1016/j.icarus.2016.06.006).
- [30] E. Mazarico, G. A. Neumann, M. K. Barker, S. Goossens, D. E. Smith, and M. T. Zuber, "Orbit determination of the lunar reconnaissance orbiter: Status after seven years," *Planet. Space Sci.*, vol. 162, pp. 2–19, Nov. 2018, doi: [10.1016/j.pss.2017.10.004](https://doi.org/10.1016/j.pss.2017.10.004).
- [31] E. Mazarico et al., "Orbit determination of the lunar reconnaissance orbiter," *J. Geodesy*, vol. 86, pp. 193–207, 2012, doi: [10.1007/s00190-011-0509-4](https://doi.org/10.1007/s00190-011-0509-4).
- [32] H. Araki, H. Noda, S. Tazawa, Y. Ishihara, S. Goossens, and S. Sasaki, "Lunar laser topography by LALT on board the KAGUYA lunar explorer – Operational history, new topographic data, peak height analysis of laser echo pulses," *Adv. Space Res.*, vol. 52, no. 2, pp. 262–271, Jul. 2013, doi: [10.1016/j.asr.2013.02.018](https://doi.org/10.1016/j.asr.2013.02.018).
- [33] D. D. Rowlands, D. E. Pavlis, F. G. Lemoine, G. A. Neumann, and S. B. Luthcke, "The use of laser altimetry in the orbit and attitude determination of Mars Global Surveyor," *Geophys. Res. Lett.*, vol. 26, no. 9, pp. 1191–1194, May 1999, doi: [10.1029/1999GL900223](https://doi.org/10.1029/1999GL900223).
- [34] M. K. Barker et al., "In-flight characterization of the lunar orbiter laser altimeter instrument pointing and far-field pattern," *Appl. Opt.*, vol. 57, no. 27, pp. 7702–7713, Sep. 2018, doi: [10.1364/AO.57.007702](https://doi.org/10.1364/AO.57.007702).
- [35] W. Hu, K. Di, Z. Liu, and J. Ping, "A new lunar global DEM derived from Chang'E-1 laser altimeter data based on crossover adjustment with local topographic constraint," *Planet. Space Sci.*, vol. 87, pp. 173–182, Oct. 2013, doi: [10.1016/j.pss.2013.08.004](https://doi.org/10.1016/j.pss.2013.08.004).
- [36] S. Goossens, E. Mazarico, Y. Ishihara, B. Archinal, and L. Gaddis, "Improving the geometry of Kaguya extended mission data through refined orbit determination using laser altimetry," *Icarus*, vol. 336, Jan. 2020, Art. no. 113454, doi: [10.1016/j.icarus.2019.113454](https://doi.org/10.1016/j.icarus.2019.113454).
- [37] M. K. Barker, E. Mazarico, G. A. Neumann, M. T. Zuber, J. Haruyama, and D. E. Smith, "A new lunar digital elevation model from the lunar orbiter laser altimeter and SELENE Terrain camera," *Icarus*, vol. 273, pp. 346–355, 2016, doi: [10.1016/j.icarus.2015.07.039](https://doi.org/10.1016/j.icarus.2015.07.039).
- [38] M. K. Barker, E. Mazarico, G. A. Neumann, D. E. Smith, M. T. Zuber, and J. W. Head, "Improved LOLA elevation maps for south pole landing sites: Error estimates and their impact on illumination conditions," *Planet. Space Sci.*, vol. 203, 2021, Art. no. 105119, doi: [10.1016/j.pss.2020.105119](https://doi.org/10.1016/j.pss.2020.105119).
- [39] E. Mazarico, G. Neumann, D. Smith, M. Zuber, and M. Torrence, "Illumination conditions of the lunar polar regions using LOLA topography," *Icarus*, vol. 211, no. 2, pp. 1066–1081, 2011, doi: [10.1016/j.icarus.2010.10.030](https://doi.org/10.1016/j.icarus.2010.10.030).
- [40] M. B. Houghton, C. R. Tooley, and R. S. Saylor Jr., "Mission design and operations considerations for NASA's lunar reconnaissance orbiter," in *Proc. 58th Int. Astronautical Congr.*, 2007, pp. 24–28.
- [41] R. Vondrak, J. Keller, G. Chin, and J. Garvin, "Lunar Reconnaissance orbiter (LRO): Observations for lunar exploration and science," *Space Sci. Rev.*, vol. 150, no. 1–4, pp. 7–22, 2010.
- [42] P. Huber, "Robust regression: Asymptotics, conjectures and Monte Carlo," *Ann. Statist.*, pp. 799–821, 1973.
- [43] M. A. Kreslavsky, J. W. Head, G. A. Neumann, M. T. Zuber, and D. E. Smith, "Low-amplitude topographic features and textures on the Moon: Initial results from detrended lunar orbiter laser altimeter (LOLA) topography," *Icarus*, vol. 283, pp. 138–145, 2017, doi: [10.1016/j.icarus.2016.07.017](https://doi.org/10.1016/j.icarus.2016.07.017).
- [44] M. A. Rosenburg et al., "Global surface slopes and roughness of the Moon from the lunar orbiter laser altimeter," *J. Geophys. Res. Planet.*, vol. 116, Feb. 2011, Art. no. E02001, doi: [10.1029/2010je003716](https://doi.org/10.1029/2010je003716).



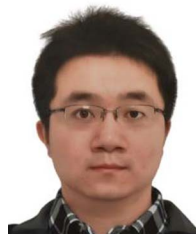
**Huan Xie** (Senior Member, IEEE) received the B.S. degree in surveying engineering, and the M.S. and Ph.D. degrees in cartography and geoinformation from Tongji University, Shanghai, China, in 2003, 2006, and 2009, respectively.

From 2007 to 2008, she was with the Institute of Photogrammetry and GeoInformation, Leibniz Universität Hannover, Germany, funded by the China Scholarship Council, as a Visiting Scholar. Her research interests include satellite laser altimetry and hyperspectral remote sensing.



**Xiaoshuai Liu** received the B.S. and M.S. degrees in mapping and surveying from Tongji University, Shanghai, China, in 2018 and 2022, respectively.

His research interests include satellite laser altimetry and topography mapping.



**Yusheng Xu** was born in 1989. He received the B.S. and M.E. degrees from Tongji University, Shanghai, China, in 2011 and 2014, respectively, and the Ph.D. (Dr.-Ing., *summa cum laude*) degree in photogrammetry and his habilitation (*venia legendi*) in point cloud analysis from the Technical University of Munich (TUM), Munich, Germany, in 2019 and 2022, respectively.

From May 2022, he joined the College of Surveying and Geoinformatics in Tongji University, Shanghai, China. He served as the guest editor or editorial

board member of several academic journals, and has authored or coauthored more than 40 entries. His research interests include three-dimensional point cloud processing, image processing, and spaceborne photogrammetry.



**Zhen Ye** (Member, IEEE) received the Ph.D. degree in photogrammetry and remote sensing from Tongji University, Shanghai, China, in 2018.

He was a Postdoctoral Researcher with the Chair of Photogrammetry and Remote Sensing, Technical University of Munich, Munich, Germany, from 2018 to 2020. He is currently an Associate Professor with the College of Surveying and Geo-informatics, Tongji University. His research interests include photogrammetry and remote sensing, high-accuracy image registration, and high-resolution satellite image processing.



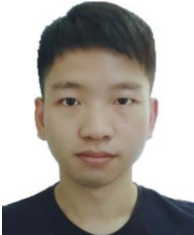
**Shijie Liu** (Member, IEEE) received the B.S. degree in surveying engineering, and the M.S. and Ph.D. degrees in cartography and geoinformation from Tongji University, Shanghai, China, in 2005, 2008, and 2012, respectively.

He is currently an Associate Professor of photogrammetry and remote sensing with the College of Surveying and Geoinformatics, Tongji University. His research interests include geometric exploitation of high-resolution remote sensing and its applications.



**Xin Li** received the M.S. degree in mapping and surveying from Tongji University, Shanghai, China, in 2022.

His research interests include lunar orbiter image processing and terrain generation.



**Binbin Li** received the Ph.D. degree in photogrammetry and remote sensing from the College of Surveying and Geo-Informatics, Tongji University, Shanghai, China, in 2022.

His current research interests include satellite laser altimetry and image processing for high-resolution satellite images.



**Qi Xu** was born in Shandong Province, China, in 1997. He received the B.S. degree in geographic information science from the Nanjing University of Posts and Telecommunications, Nanjing, China, in 2015. He is currently working toward the Ph.D. degree in photogrammetry and remote sensing from Tongji University, Shanghai, China.

His research interests include satellite single-photon data processing and applications.



**Yalei Guo** received the M.S. degree in photogrammetry and remote sensing from the College of Surveying and Geo-Informatics, Tongji University, Shanghai, China, in 2022.

His current research interests include On-orbit calibration of satellite single-photon laser altimeter



**Xiaohua Tong** (Senior Member, IEEE) received the Ph.D. degree in traffic engineering from Tongji University, Shanghai, China, in 1999.

From 2001 to 2003, he was a Postdoctoral Researcher with the State Key Laboratory of Information Engineering, Surveying, Mapping, and Remote Sensing, Wuhan University, Wuhan, China. He was a Research Fellow with Hong Kong Polytechnic University, Hong Kong, in 2006, and a Visiting Scholar with the University of California, Santa Barbara, CA, USA, from 2008 to 2009. His research interests include

photogrammetry and remote sensing, trust in spatial data, and image processing for high-resolution satellite images.